Quantum Electronics **36** (10) 918 – 924 (2006) ©2006 Kvantovaya Elektronika and Turpion Ltd

LASERS

PACS numbers: 42.55.Px; 42.60.Lh
DOI: 10.1070/QE2006v036n10ABEH013278

Simulations of light – current and spectral characteristics of InGaAlAs/InP semiconductor lasers

A.V. Ivanov, V.D. Kurnosov, K.V. Kurnosov,
V.I. Romantsevich, Yu.A. Ryaboshtan, R.V. Chernov

***Abstract*. The light – current and spectral characteristics of semiconductor lasers are simulated by using models with and without inverse mass for radiative transitions with and without fulfilment of the wave-vector selection rules. The best agreement between the theory and experiment is obtained for a model without inverse mass with radiative transitions without fulfilment of the selection rules. The obtained results are discussed.**

Keywords: *semiconductor lasers, model with and without inverse mass, radiative transitions with and without fulfilment of the selection rules.*

1. Introduction

The growth of multilayer quantum-well heterostructures and fabrication of semiconductor quantum-well lasers (QWLs) from them is a complicated and expensive process. Therefore, the choice of a model that would adequately describe the light – current and spectral parameters of QWLs is an important problem of current interest. The characteristics of QWLs were simulated in many papers which, however, were mainly devoted to the calculation of the gain, although the developers of these devices are interested first of all in the energy and spectral characteristics of QWLs.

Our paper is devoted to the simulation of these characteristics of a QWL. We considered two models: with and without inverse mass. In turn, in each of these models we considered radiative transitions occurring with and without fulfilment of the wave-vector selection rules.

We assume that quantum-well layers are grown in the {100} plane. Then, the model with inverse mass considers the longitudinal (along the growth direction) components of masses of heavy and light holes, which are denoted as m_{vh} and m_{vl}, respectively, and the transverse components (in the quantum-well plane), which are denoted as m_{vht} and m_{vlt}, respectively. In this case, heavy holes have a smaller mass than light holes. This effect is known as the inverse mass [1].

The longitudinal mass components m_{vh} and m_{vl} are used for calculations of the dimensional quantisation levels, while the transverse components m_{vht} and m_{vlt} (determining the state density) are used to calculate the gain and the density of carriers in wells.

In the model without inverse mass, the dimensional quantisation levels, the gain, and the density of carriers in wells are calculated by using mass components coinciding with the longitudinal mass components m_{vh} and m_{vl} of heavy and light holes.

Earlier, the model without inverse mass was used in calculations; however, recently the inverse-mass model has received wide acceptance. The inverse-mass model was used for calculations of QWLs, for example, in papers [2 – 4], while the model without inverse mass was applied in [5 – 7]. Processes of radiative recombination with and without the fulfilment of the selection rules were considered in detail in papers [8, 9].

In this paper, we calculated the power and spectral characteristics of QWLs by using the quantities x and y determining compositions of the $In_{1-x-y}Ga_yAl_xAs$ layers of active regions (quantum wells), barrier and waveguide layers. The energy gap widths and dimensional quantisation levels were calculated from technological values of x and y for quantum wells and barrier layers and their geometrical sizes. The dimensional quantisation levels in wells were calculated taking into account a change in the energy gap width due to its filling with free carriers.

We did not consider in our study an increase in the emission wavelength and switching of radiation modes caused by the heating of carriers with increasing the pump current. The calculation of characteristics taking into account the heating of carriers is rather time-consuming, however, as shown in [10], this calculation does not change light – current characteristics, and the emission wavelength at the lasing threshold coincides with that calculated by neglecting the heating of carriers.

2. Parameters of heterostructures under study and characteristics of lasers based on them

To calculate the characteristics of QWLs, we used the $In_{1-x-y}Ga_yAl_xAs$ layers with $x_a = 0.11$ and $y_a = 0.37$ for the active region and $x_b = 0.31$ and $y_b = 0.17$ for barrier and waveguide layers. Four quantum wells 60 Å thick each were grown, between which three barrier layers 130 Å thick each were located. To the right and left of the extreme

A.V. Ivanov, V.D. Kurnosov, K.V. Kurnosov, V.I. Romantsevich, Yu.A. Ryaboshtan, R.V. Chernov M.F. Stel'makh Polyus Research & Development Institute, ul. Vvedenskogo 3, 117342 Moscow, Russia; e-mail: dilas@mail.magelan.ru, webeks@mail.ru, juri@siplus.ru

Received 28 March 2006; revision received 24 May 2006
Kvantovaya Elektronika **36** (10) 918 – 924 (2006)
Translated by M.N. Sapozhnikov

wells, waveguide layers of thickness 0.08 μm each were located. The active regions, barrier and waveguide layers were undoped. The conduction-band discontinuity energy ΔE_c was set equal to $0.72\Delta E_g$, where ΔE_g is the difference of the energy gap widths of the active region and waveguide layers [11].

Mesastripe laser diodes with the stripe of width 2 μm were fabricated from this heterostructure. We selected lasers with resonators of length 200 and 400 μm for investigations. The reflecting and antireflection coatings with reflection coefficients 80 % and 15 %, respectively, were deposited on the resonator facets. The output power was measured for radiation emitted from the resonator facet with the 15 % coating. The calculated optical confinement factor for the active region is $\Gamma_a = N_{qw}\Gamma_{a\,qw} = 0.0366$, where $N_{qw} = 4$ is the number of quantum wells and $\Gamma_{a\,qw}$ is the optical confinement factor for a quantum well. The optical confinement factor Γ_b of waveguide layers was 0.286.

The longitudinal and transverse masses of heavy and light holes were calculated by using the Luttinger–Kohn parameters γ_1 and γ_2 [1]. The intraband relaxation time of carriers was set equal to 0.4×10^{-13} s.

The spectral parameters of semiconductor lasers strongly depend on the radiation power reflected back to the laser. To avoid this, an optical isolator was placed in front of an optical spectrum analyser, which suppressed the signal reflected back by ~60 dB. Measurements were performed by using a single-mode fibre whose output end facing the laser was melted to form a cone with a microlens of diameter ~2 μm at its end. An FC/APC connector was set at another end of the fibre. To reduce additionally the power of the signal reflected back, the single-mode fibre with the microlens was placed at such a distance from the resonator that for 5 mW of output power of the laser the radiation power in the fibre was ~0.1 mW. This power was sufficient to detect a signal with an optical spectrum analyser.

Figure 1 presents experimental light–current characteristics and dependences of the laser wavelength, corresponding to the maximum of the emission spectrum envelope, on the pump current in pulsed and cw regimes. The pulse duration and repetition rate were 50 ns and 300 kHz, respectively. Note that, although efforts were taken to eliminate optical feedback, upon cw current pumping in the current range from 23 to 30 mA, unstable lasing was observed in a QWL with the resonators length $L = 400$ μm caused by spontaneous mode switching.

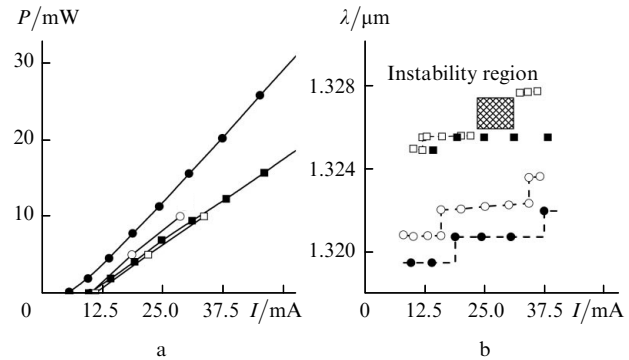

Figure 1. Experimental light–current characteristics (a) and dependences of the emission wavelength (b) for lasers in the pulsed [the resonator length is $L = 200$ (●) and 400 μm (■)] and cw [$L = 200$ (○) and 400 μm (□)] regimes.

Upon pulsed pumping, the emission spectrum of the same QWL was stable. For a QWL with $L = 200$ μm, the pulsed pump current was lower that the pump current in the cw regime, whereas for the laser with the resonator length of 400 μm these currents almost coincided. The difference in the pump currents is reflected in the spectral characteristics presented in Fig. 1b. The emission wavelength in the pulsed regime for the QWL with $L = 200$ μm is shorter than that in the cw regime.

The pulsed optical power was measured with a fast stroboscopic oscilloscope and a photodiode with the passband more than 10 GHz. Because no coupling capacitors were used in the circuit, the photodiode was calibrated by using a constant pump current corresponding to 5 mW of the output power. The deviation of the oscilloscope beam upon applying a constant pump current was compared with the optical pulse amplitude observed upon pulsed current pumping.

3. Expressions for calculations

As mentioned above, the dimensional quantisation levels were calculated in the inverse-mass model by using the longitudinal mass components of heavy and light holes:

$$m_{vh} = \frac{m_0}{\gamma_1 - 2\gamma_2}, \quad m_{vl} = \frac{m_0}{\gamma_1 + 2\gamma_2}. \tag{1}$$

The density of states in quantum wells is calculated by using the transverse mass components of heavy and light holes:

$$m_{vht} = \frac{m_0}{\gamma_1 + \gamma_2}, \quad m_{vlt} = \frac{m_0}{\gamma_1 - \gamma_2}. \tag{2}$$

The Luttinger–Kohn parameters γ_1 and γ_2 were calculated from interpolation formulas [11]:

$$\gamma_1(\mathrm{In}_{1-x-y}\mathrm{Ga}_y\mathrm{Al}_x\mathrm{As}) = \gamma_1(\mathrm{InAs})(1 - x - y) + \gamma_1(\mathrm{GaAs})y + \gamma_1(\mathrm{AlAs})x, \tag{3}$$

where the values of γ_1 for InAs, GaAs, AlAs were taken from Table 1 [11]. The values of γ_2 were calculated similarly.

The effective electron mass was calculated from the expression similar to (3); in this case, the deviation from the value calculated from the expression [12]

$$m_c = 0.0427 + 0.0683x \tag{4}$$

was no more than 10 %.

In the model of radiative transitions with the fulfilment of the wave-vector selection rules, the gains and rates of spontaneous transitions are deermined by the expressions [13, 14]

$$g(h\nu) = \sum_{n,i} \int \frac{A_{cv}}{\pi\hbar^2 v_{gr}\rho L_a} \times m_{ri}\left[f_c(\mathscr{E}_{cni}) - f_v(\mathscr{E}_{vni})\right] L(h\nu, E_{cv})\mathrm{d}E_{cv}, \tag{5}$$

$$r_{\rm cp}(h\nu) = \sum_{n,i} \int \frac{A_{\rm cv}}{\pi\hbar^2 L_{\rm a}} \times m_{{\rm r}i} f_{\rm c}(\mathscr{E}_{{\rm c}ni}) \left[1 - f_{\rm v}(\mathscr{E}_{{\rm v}ni})\right] L(h\nu, E_{\rm cv}) {\rm d}E_{\rm cv}, \quad (6)$$

where

$$\mathscr{E}_{{\rm c}ni} = E_{\rm c0} + \frac{m_{{\rm r}i}}{m_{\rm c}}(E_{\rm cv} - E_{\rm g}) + \frac{m_{{\rm r}i}}{m_{{\rm v}it}} E_{{\rm c}n} - \frac{m_{{\rm r}i}}{m_{\rm c}} E_{{\rm v}in};$$

$$\mathscr{E}_{{\rm v}ni} = E_{\rm v0} + \frac{m_{{\rm r}i}}{m_{{\rm v}it}}(E_{\rm cv} - E_{\rm g}) + \frac{m_{{\rm r}i}}{m_{{\rm v}it}} E_{{\rm c}n} - \frac{m_{{\rm r}i}}{m_{\rm c}} E_{{\rm v}in}; \quad (7)$$

$h\nu$ is the photon energy; A is the Einstein coefficient; ρ is the density of modes of the electromagnetic field in a crystal; $L_{\rm a}$ is the active-region thickness; $m_{\rm c}$ is the effective electron mass; $m_{{\rm v}it}$ are the transverse components of the effective masses of light and heavy holes; $m_{{\rm r}i} = m_{\rm c} m_{{\rm v}it}/(m_{\rm c} + m_{{\rm v}it})$ is the reduced mass taking into account the corresponding holes; $v_{\rm gr}$ is the group speed of light; and $f_{\rm c}(\mathscr{E}_{{\rm c}ni})$ and $f_{\rm v}(\mathscr{E}_{{\rm v}ni})$ are the Fermi–Dirac functions (subscripts $i = {\rm h}, {\rm l}$ refer to heavy and light holes, n is the subband number). The lower integration limit in (5) and (6) is set equal to $h\nu_{ni} = E_{\rm ga} + E_{{\rm c}n} + E_{{\rm v}in}$ and corresponds to the energy of initial transitions for subbands with the number n. Here, $E_{\rm ga} = E_{\rm ca} - E_{\rm va}$, where $E_{\rm ca}$ and $E_{\rm va}$ are the bottom of the conduction band and the top of the valence band in the active region, respectively; $E_{{\rm c}n}$ are the ground states of electron subbands; and $E_{{\rm v}in}$ are the ground states of hole subbands, which are determined by the longitudinal components $m_{{\rm v}il}$ of the effective masses of holes. The upper integration limit is limited by the height of potential barriers in a quantum well.

The broadening of the emission line is described by a Lorentzian

$$L(h\nu - E_{\rm cv}) = \frac{1}{\pi} \frac{\Gamma_{\rm cv}}{(h\nu - E_{\rm cv})^2 + \Gamma_{\rm cv}^2}, \quad (8)$$

where $\Gamma_{\rm cv} = \hbar/\tau_{\rm in}$; $\tau_{\rm in}$ is the intraband relaxation time of carriers and $2\Gamma_{\rm cv}$ is the emission linewidth.

The averaged square of the matrix element of the band-band transitions entering $A_{\rm cv}$ is defined as

$$|M|^2 = \alpha_{ni} |M_{\rm cv}|^2,$$

where

$$|M_{\rm cv}|^2 = \frac{m_0 E_{\rm ga}(E_{\rm ga} + \Delta)}{6 m_{\rm c}(E_{\rm ga} + 2\Delta/3)}.$$

The spin–orbit splitting energy Δ is found from the expression similar to (3). The coefficient α_{ni} characterising the 'polarisation' dispersion for the TE mode and transitions to the levels of heavy and light holes is determined by the expression [4, 13]

$$\alpha_{n{\rm h}} = \frac{3}{4}\left[1 + \cos^2\theta\right], \quad \alpha_{n{\rm l}} = \frac{1}{4}\left[5 - 3\cos^2\theta\right], \quad (9)$$

where $\cos^2\theta = (E_{{\rm c}n} + E_{{\rm v}in})/(E_{\rm cv} - E_{\rm g})$; θ is the angle between the dimensional quantisation axis $\langle 100 \rangle$ and the wave vector of holes.

The total rate of spontaneous recombination is

$$R_{\rm sp} = \int r_{\rm sp}(h\nu) {\rm d}h\nu, \quad (10)$$

where $r_{\rm sp}(h\nu)$ is found from (6), the lower integration limit in (10) is set equal to $E_{\rm ga} + E_{\rm c1} + E_{\rm v1h}$, and the upper integration limit is restricted by the height of potential barriers in a quantum well.

The Fermi quasi-levels $F_{\rm c}$ and $F_{\rm v}$ in the conduction and valence bands, respectively, are related by the electric-neutrality equation [15]

$$N_{\rm qw} L_{\rm a}(n_{\rm a} - p_{\rm a}) + L_{\rm b}(n_{\rm b} - p_{\rm b}) = 0, \quad (11)$$

where $n_{\rm a}(F_{\rm c})$ and $p_{\rm a}(F_{\rm v})$ are the electron and hole concentrations in the active region of thickness $L_{\rm a}$; $n_{\rm b}(F_{\rm c})$ and $p_{\rm b}(F_{\rm v})$ are concentrations of carriers in the waveguide layer; and $L_{\rm b}$ is the waveguide layer.

The electron and hole densities in the active region of the laser are described by the expressions

$$n_{\rm a} = \rho_{\rm c} kT \sum_n \ln\left\{\frac{1 + \exp[(F_{\rm c} - E_{\rm ca} - E_{{\rm c}n})/kT]}{1 + \exp[(F_{\rm c} - E_{\rm cb})/kT]}\right\},$$

$$p_{\rm a} = kT \sum_{n,i} \rho_{{\rm v}it} \ln\left\{\frac{1 + \exp[(E_{\rm va} - E_{{\rm v}in} - F_{\rm v})/kT]}{1 + \exp[(E_{\rm vb} - F_{\rm v})/kT]}\right\}, \quad (12)$$

where $\rho_{\rm c} = m_{\rm c}/(\pi\hbar^2 L_{\rm a})$ and $\rho_{{\rm v}it} = m_{{\rm v}it}/(\pi\hbar^2 L_{\rm a})$ are the effective densities of states ($i = {\rm h}, {\rm l}$); $E_{\rm cb}$ and $E_{\rm vb}$ are the bottom of the conduction band and the top of the valence band in the waveguide region, respectively. The concentrations of carriers in the waveguide layer are described by the expressions

$$n_{\rm b}(F_{\rm c}) = \int_{E_{\rm cb}}^{E_{\rm cem}} \rho_{\rm bc}(E) f_{\rm c}(E) {\rm d}E,$$

$$p_{\rm b}(F_{\rm v}) = \sum_i \int_{E_{\rm vem}}^{E_{\rm vb}} \rho_{{\rm bv}i}(E)[1 - f_{\rm v}(E)] {\rm d}E, \quad (13)$$

where $\rho_{\rm bc}$ and $\rho_{{\rm bv}i}$ are the effective densities of states in the waveguide layer [9]; and $E_{\rm cem}$ and $E_{\rm vem}$ are the energies of the bottom of the conduction band and the top of the valence band in the emitter layer.

We took into account in calculations the narrowing of the energy gap widths $E_{\rm ga}$ and $E_{\rm gb}$ in $In_{1-x-y}Ga_yAl_xAs$ in the active region and waveguide layers, respectively, upon pumping the laser structure by current ($i = {\rm a}, {\rm b}$):

$$E_{{\rm g}i} = E_{\rm g}(x_i, y_i) - k_{\rm g}\left(n_i^{1/3} + p_i^{1/3}\right). \quad (14)$$

The energy gap width $E_{\rm g}(x, y)$ in the unstrained layers of $In_{1-x-y}Ga_yAl_xAs$ in the absence of current pumping was calculated from the expression [11]

$$E_{\rm g}(x, y) = 0.36 + 2.093x + 0.629y + 0.577x^2 + 0.436y^2 + 1.013xy - 2xy(1 - x - y). \quad (15)$$

In the stationary case, the volume photon densities S_m in the mth mode with the energy E_m are described by the expression [16, 17]

$$v_{gr}(G_m - \alpha)S_m + \beta R_{sp} = 0, \tag{16}$$

where $G_m = \Gamma_a g(E_m) - \varepsilon_m S_m - \sum_{q \neq m} D_q S_q$; Γ_a is the optical confinement factor in the active region; and β is the coefficient taking into account the contribution of spontaneous radiation to the generated mode.

Coefficients ε_m and D_q have the form [17]

$$\varepsilon_m = \frac{9}{4}\frac{E_m \Gamma_a \alpha}{\varepsilon^{(0)} n_{gr}^2}\left(\frac{\tau_{in}}{\hbar}\right)^2 \langle R_{cv}^2 \rangle,$$

$$D_q = \frac{4}{3}\frac{\varepsilon_m}{1 + (\tau_{in} 2\pi v_q/\lambda_q)^2(\lambda_m - \lambda_q)^2}, \tag{17}$$

where $\langle R_{cv}^2 \rangle$ is the dipole moment; n_{gr} is the group refractive index; $\varepsilon^{(0)}$ is the dielectric constant; and λ_m and λ_q are the wavelengths of the mth and qth modes, respectively. The losses in the laser are [9]

$$\alpha = \alpha_0 + L^{-1} \ln \frac{1}{\sqrt{R_1 R_2}}$$

$$+ \Gamma_a \alpha_a + \Gamma_b \alpha_b + (1 - \Gamma_a - \Gamma_b)\alpha_{em}, \tag{18}$$

where α_0 are nonresonance losses; L is the laser resonator length; and R_1 and R_2 are the reflection coefficients of mirrors. The losses on free carriers in the active region, waveguide, and emitter layers are

$$\alpha_i = \sigma_e n_i + \sigma_h p_i, \tag{19}$$

where $i =$ a, b, em; n_a and p_a, n_b and p_b, and n_{em} and p_{em} are the densities of carriers in the active region and waveguide and emitter layers, respectively (n_{em} and p_{em} are determined by the doping level of N- and P-emitters); σ_e and σ_h are the absorption cross sections for electrons and holes, respectively.

The optical power emitted from one facet of the resonator is described by the expression

$$P = \sum_m P_m = \frac{1}{2} h\nu \frac{V_a}{L} v_{gr} \ln \frac{1}{R_1 R_2}$$

$$\times \frac{1 - R_1}{1 - R_1 + \sqrt{R_1/R_2}(1 - R_2)} \sum_m S_m, \tag{20}$$

where P_m is the radiation power of the mth mode and V_a is the active region volume.

The pump current is described by the expression

$$I = qV_a\left(R_a + v_{gr}\sum_m G_m S_m\right) + qV_b R_b, \tag{21}$$

where V_b is the volume of waveguide layers. The total rate of radiative and nonradiative recombination in the active region (R_a) and waveguide layers (R_b) ($i =$ a, b) is

$$R_i = An_i + R_{spi} + C_n n_i^2 p_i + C_p n_i p_i^2, \tag{22}$$

where A, C_n, and C_p are constants. The rate R_{spb} of spontaneous recombination of carriers in waveguide layers is determined by expression (10) in which the rate $r_{spb}(h\nu)$ of spontaneous transitions in the waveguide region is taken for a bulk semiconductor [9], integration is performed from the energy gap width E_{gb} of the waveguide layer to the energy gap width E_{gem} of the emitter layer.

The gain in the model of transitions without the fulfilment of the wave-vector selection rules is determined by the expression [18, 19]

$$g(h\nu) = \frac{A_1}{v_{gr}\phi(h\nu)(\pi\hbar^2 L_a)^2}\sum_{n,i}\int_{E_{cn}}^{E_{vni}+h\nu} m_c m_{vi}\left[f_c(E) - f_v(E - h\nu)\right]dE$$

$$= G_0 \sum_i \sum_{n,k}\left\{m_{hi}\ln\left[\frac{1 + \exp[(F_c - h\nu - E_{vni})/kT]}{1 + \exp[(F_c - E_{cni})/kT]} \times \frac{1 + \exp[(F_v + h\nu - E_{cki})/kT]}{1 + \exp[(F_v - E_{vki})/kT]}\right]\right\}, \tag{23}$$

where

$$G_0 = -\frac{\pi e^2 \hbar}{m_0^2 \varepsilon_0 n_a c h\nu}\frac{m_c kT}{(\pi\hbar^2 L_a)^2} 4\pi a_0^2 L_a |M|^2;$$

$A_1 = 4\pi a_0^2 L_a A_{cv}$; $E_{cni} = E_{c0} + E_{cn}$, $E_{vni} = E_{v0} - E_{vin}$; $i =$ h, l; the subscripts n and k in summation are the numbers of subbands in the quantum well; a_0 is the effective Bohr radius of the impurity; and n_a is the refractive index. Coefficients α_{ni} characterising 'polarisation' dispersion for the TE mode and transitions to the levels of heavy and light holes were set equal to $\alpha_{nh} = 1.296$ and $\alpha_{nl} = 0.524$. These values were calculated by expression (9) for the energy corresponding to the lasing threshold of the QWL.

The rate of spontaneous transitions can be expressed in terms of the gain as

$$r_{sp}(h\nu) = \frac{8\pi(n_a h\nu)^2}{h^3 c^2\{\exp\{[h\nu - (F_c - F_v)]/kT\} - 1\}}[-g(h\nu)]. \tag{24}$$

4. Comparison of calculation and experimental results

Let us compare calculation and experimental results. Because the temperature dependence of the energy gap width for the active region of an InGaAlAs/InP QWL is unknown, we will compare the results of calculations with experimental results obtained for the pulsed pump regime of the QWL. We assume that the temperature of the active region of the laser coincides with the temperature of the environment. We also assume in calculations that $\tau_{in} = 4 \times 10^{-14}$ s, $C_n = C_p = 5 \times 10^{-29}$ cm^6 s^{-1}, and $\alpha_0 = 25$ cm^{-1}.

Figure 2 presents the results of calculation of the QWL characteristics in the inverse-mass model. The results obtained for the model with and without the fulfilment of the wave-vector selection rules are shown at the left and right, respectively.

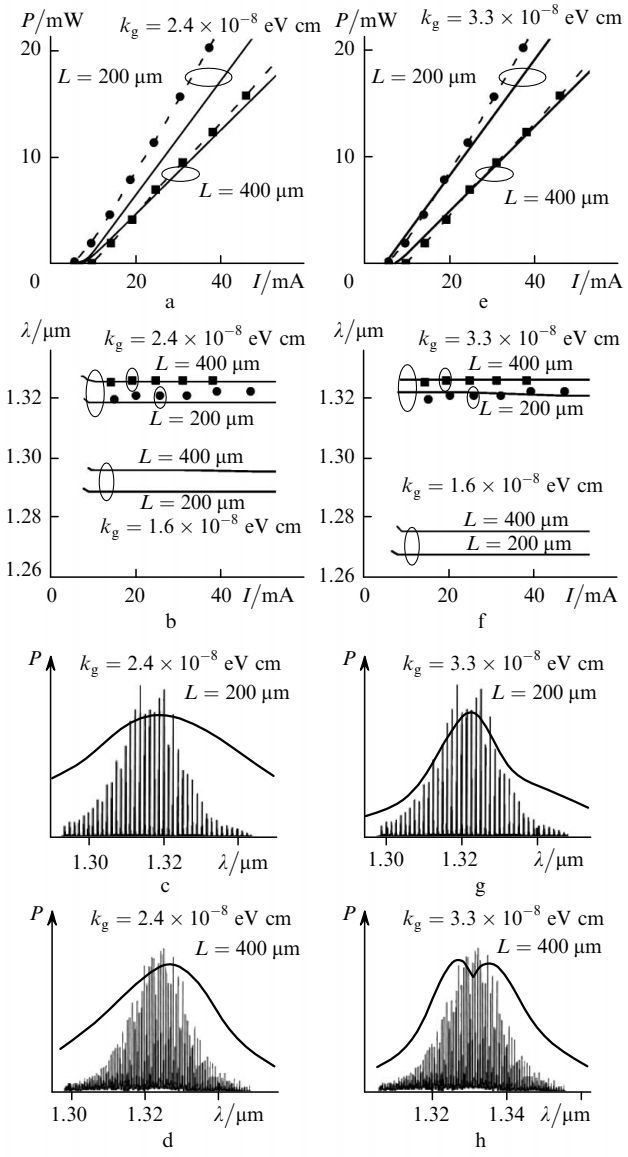

Figure 2. Light–current (a, e) and spectral (b, f) characteristics, and emission spectra below the lasing threshold (c, g) calculated by using the inverse-mass model with (a–d) and without (e–h) fulfilment of the wave-vector selection rules for laser diodes with $L = 200$ and 400 μm for different values of k_g. Squares and circles are experimental values, solid curves are calculations (a, b, e, f).

The coefficients C_n and C_p (22) determining the Auger recombination currents in the laser and the coefficient k_g in (14) were used as fitting parameters to provide the agreement between calculated and experimental light–current characteristics and between the calculated and experimental dependences of the QWL wavelength on the pump current. Therefore, to compare the theory with experiment, it is necessary to use lasers with resonators of different lengths. This is explained by the fact that while the agreement between the calculated and experimental threshold current (spectrum) can be obtained for one chosen length of the resonator, this agreement can be absent for the resonator of different length with coefficients C_n, C_p, and k_g selected in the former case.

One can see from Fig. 2a that the calculated light–current characteristics differ from experimental characteristics, whereas the threshold currents for QWLs with resonators of lengths 200 and 400 μm almost coincide, which contradicts the experiment.

The dependences of the emission wavelength, corresponding to the maximum of the spectrum envelope, on the pump current above the lasing threshold presented in Fig. 2b coincide with the experimental dependences if we set $k_g = 2.4 \times 10^{-8}$ eV cm. These dependences in Fig. 2b are also shown for $k_g = 1.6 \times 10^{-8}$ eV cm. By comparing the calculated emission lines of QWLs with $L = 200$ and 400 μm below the lasing threshold (solid curves), we see that they are broadened and do not coincide with the experimental spectra (Figs 2c, d).

Thus, we can conclude that in the case of fulfilment of the wave-vector selection rules, the inverse-mass model inadequately describes experimental results.

Consider now the results of calculations in the inverse-mass model when the wave-vector selection rules are not fulfilled. The results presented in Figs 2e–h show that the calculated light–current characteristics and dependences of the emission wavelength on the pump current above the lasing threshold well agree with the corresponding experimental data if we assume that $k_g = 3.3 \times 10^{-8}$ eV cm. However, the calculated spectral characteristics below the lasing threshold (Figs 2g, h) poorly describe experiments for this value of k_g.

Figure 3 presents the results of simulation of QWL parameters in the model without inverse mass. As in Fig. 2, the results obtained for the model with and without fulfilment of the selection rules are given at the left and right, respectively. One can see from Fig. 3a that, as in Fig. 2a, the experimental and theoretical light–current characteristics are inconsistent. This also concerns spectral characteristics obtained below the lasing threshold (Figs 3c, d).

Thus, we can conclude that in the case of fulfilment of the wave-vector selection rules, the model without inverse mass also inadequately describes experimental results.

Finally, we consider the QWL characteristics calculated in the model without inverse mass when the wave-vector selection rules are not fulfilled.

Analysis of the results presented in Figs 3e–h shows that this model provides the best agreement with experiment data among the results presented in Figs 2 and 3.

5. Discussion of the results

Let us find the reason why the model without inverse mass with radiative transitions without fulfilment of the selection rules provides the best agreement with experiments. For this purpose, we will analyse the shape of the gain in the inverse-mass model at different intraband relaxation times τ_{in} of carriers.

Figure 4 presents the gains of a QWL with $L = 200$ μm calculated for $\tau_{in} = 1 \times 10^{-13}$ and 0.4×10^{-13} s for the inverse-mass model with radiative transitions with fulfilment of the selection rules; the radiation power is $P = 10$ mW. In this model, electronic transitions can occur from the levels located in the first subband of the conduction band, determined by the first quantum level in the well, to the enery levels of the first subband of heavy [curves (*1*)] and the first subband of light [curves (*2*)] holes. Also, electronic transitions can occur from the second subband in the conduction band to the second subband of heavy holes (these transitions lie outside Fig. 4). For a quantum well with $\Delta E_c/\Delta E_g = 0.72$, there exist two quantum levels in the

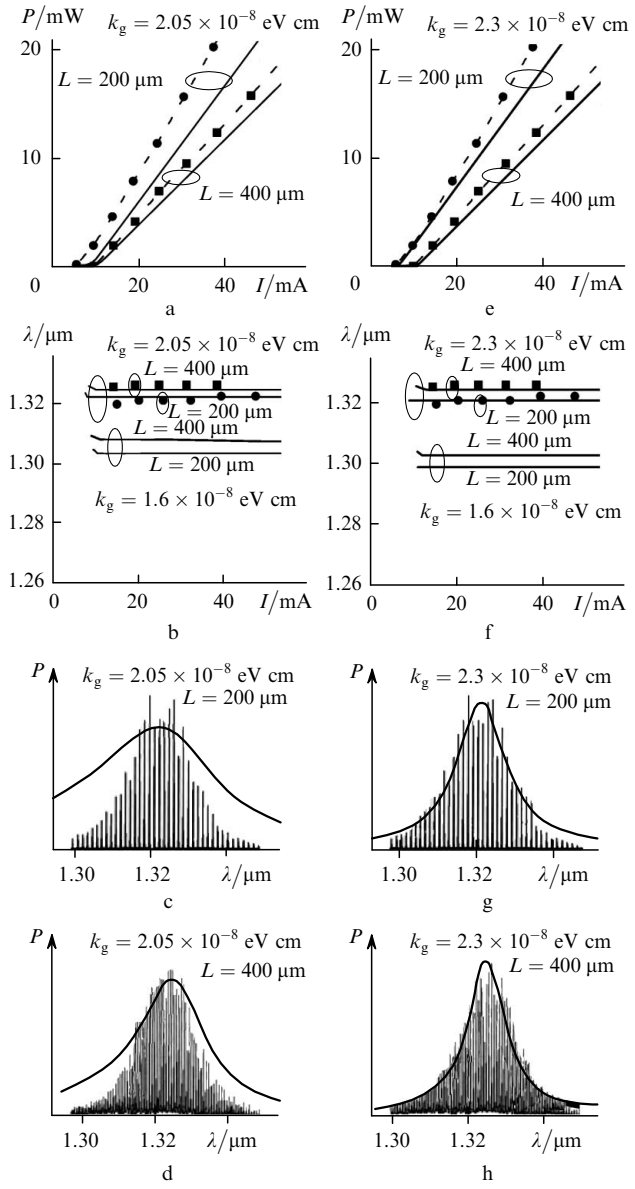

Figure 3. Light–current (a, e) and spectral (b, f) characteristics, and emission spectra below the lasing threshold (c, g) calculated by using the model without inverse mass with (a–d) and without (e–h) fulfilment of the wave-vector selection rules for laser diodes with $L = 200$ and 400 μm for different values of k_g. Squares and circles are experimental values, solid curves are calculations (a, b, e, f).

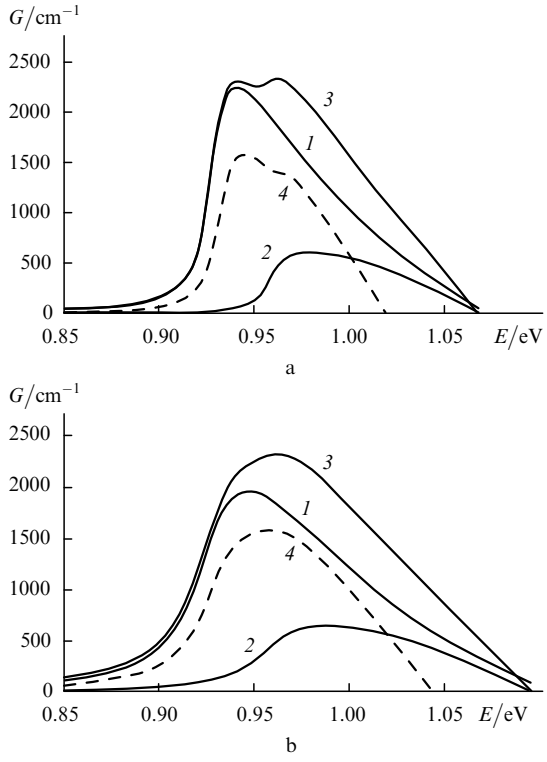

Figure 4. Dependences of the gain on the transition energy for $\tau_{in} = 1 \times 10^{-13}$ (a) and 0.4×10^{-13} s (b). Curves (*1*) and (*2*) are gains corresponding to the conduction band–heavy holes and conduction band–light holes transitions, respectively, and curve (*3*) is the total gain for the laser with $L = 200$ μm. Curve (*4*) is the total gain for the laser with $L = 400$ μm.

conduction band, which determine two subbands for electrons, and two levels for heavy holes and one level for light holes in the valence band. The second level for light holes lies outside the quantum well of the valence band. Curve (*3*) in Fig. 4 is determined by the sum of transitions shown by curves (*1*) and (*2*).

One can see from Fig. 4a that the gain for $L = 200$ μm has two maxima, which are also observed in the calculated emission spectrum below the lasing threshold, which is inconsistent with the experiment. As the intraband relaxation time τ_{in} is decreased down to 0.4×10^{-13} s, the gain band broadens and has one maximum; however, the calculated and experimental spectral characteristics are inconsistent in this case as well (Figs 2c, d).

The dashed curve in Fig. 4a presents the gain for a QWL with $L = 400$ μm. The calculation shows that lasing in a QWL with $L = 200$ μm occurs at the wavelength corresponding to the right maximum in curve (*3*) in Fig. 4a. This results in a large difference between the emission wavelengths of QWLs with $L = 200$ and 400 μm, which is inconsistent with experimental data. If lasing occurs at the left maximum of curve (*3*) (Fig. 4a), the emission wavelength of the QWL with $L = 200$ μm becomes longer than that of the QWL with $L = 400$ μm, which is also inconsistent with the experiment.

The discrepancy between the theory and experiment is explained by the dominating role of the transitions of carriers from the conduction band to the levels of light holes because the mass of light holes is greater than that of heavy holes. This gives rise to two maxima of the gain for $L = 200$ μm, which is inconsistent with experimental emission spectra.

We have chosen the value $\tau_{in} = 0.4 \times 10^{-13}$ s not due to the absence of the two maxima in the gain curve for the QWL with $L = 200$ μm (Fig. 4b) but for other reasons. The matter is that for $\tau_{in} = 1 \times 10^{-13}$ s, the model of spectral burning of carriers [see expressions (16) and (17)] leads to large discrepancies between the calculated and experimental spectral characteristics above the lasing threshold. While the experimental amplitude ratio for the lasing and neighbouring modes does not exceed 1 : 10, the calculated ratio exceeds 1 : 500. This is explained by the fact that the model of spectral burning of carriers developed in [16, 17] and explaining adequately experiments with GaAlAs/GaAs [20, 21] is not valid for InGaAlAs/InP heterostructures for the intraband relaxation time $\tau_{in} = 1 \times 10^{-13}$ s.

Thus, the model without inverse mass and without fulfilment of the wave-vector selection rules provides the best agreement with experimental data. The validity of this model for laser and superluminescent diodes is proved in [22] and [23], respectively.

In our paper, the agreement between the experimental and calculated dependences of the emission wavelength, corresponding to the maximum of the spectral envelope, on the pump current (Figs 2b, f and Fig. 3b, f) was achieved with the help of the fitting parameter k_g in (14). Figures 2b, f and 3b, f present the dependences of the emission wavelength on the pump current for $k_g = 1.6 \times 10^{-8}$ eV cm and other values of k_g for which the best agreement with experiments was obtained. One can see that the spread of values of k_g is large. At present different values of k_g are used in the literature because there is no consensus on the proper value of this coefficient.

The narrowing of the energy gap was calculated in (14) taking into account electrons and holes; therefore, if only one type of carriers is taken into account, the coefficient k_g should be doubled. In [7], the value $k_g = 3.2 \times 10^{-8}$ eV cm was used. In [24], the expression $\Delta E_g = 1.8 \times 10^{-8}(n^{1/2} + p^{1/2})$ was used (where n and p are measured in cm^{-2}), in [25] – the expression $\Delta E_g = 2.2 \times 10^{-6}(L_z n)^{0.34}$ (i.e. the dependence on the energy gap width L_z was introduced), in [26] – the expression $\Delta E_g = 1 \times 10^{-8} n^{0.34}$. In [27], the dependence $\Delta E_g = (k/\varepsilon_s)(1 - n/n_{st})^{1/3}$ was considered, where $n_{st} = 1.6 \times 10^{24} \times (m_c/1.4\varepsilon_s)^3$; ε_s is the relative dielectric constant of a semiconductor; $k = 0.11$ for p-GaAs, 0.125 for n-GaAs, and 0.14 for the electron – hole plasma in GaAs. The results of paper [28] do not differ considerably from earlier results.

Our calculations have shown that a change in the coefficient k_g results in the shift of the wavelength of the QWL (see Figs 2, 3) and almost does not affect light – current characteristics.

Note that the values of x_a and y_a are determined by technologists with an accuracy of ± 0.01; therefore, if values $x_a = 0.099$ and $y_a = 0.381$ are taken (instead of $x_a = 0.11$ and $y_a = 0.37$), the calculated spectra in Figs 3f – h will coincide with experimental spectra for $k_g = 1.6 \times 10^{-8}$ eV cm.

Thus, we believe that the power and spectral characteristics of QWLs should be simulated by using the model without inverse mass with radiative transitions without fulfilment of the wave-vector selection rules because this model provides the best agreement with experimental data.

References

1. Peter U., Cardona M. *Osnovy fiziki poluprovodnikov* (Fundamentals of Physics of Semiconductors) (Moscow: Fizmatlit, 2002).
2. Batrak D.V., Bogatova S.A., et al. *Kvantovaya Elektron.*, **35**, 316 (2005) [*Quantum Electron.*, 35, 316 (2005)].
3. Kurnosov V.D., Kurnosov K.V., Chernov R.V. *Kvantovaya Elektron.*, **32**, 303 (2002) [*Quantum Electron.*, 32, 303 (2002)].
4. Kononenko V.K., Manak I.S., Furunzhiev E.R. *Zh. Prikl. Spektr.*, **64**, 797 (1997).
5. Yamada M., Ogita S., Yamagishi M., Tabata K. *IEEE J. Quantum Electron.*, **21**, 640 (1985).
6. Zielinski E., Schweizer H., Hausser S., et al. *IEEE J. Quantum Electron.*, **23**, 969 (1987).
7. Chinn S.R., Zory P.S., Reisinger A.R. *IEEE J. Quantum Electron.*, **24**, 2191 (1988).
8. Lasher G., Stern F. *Phys. Rev.*, **133**, A553 (1964).
9. Gasey N.C. Jr., Panise M.B. *Heterostructure Lasers, Part A* (New York: Academic Press, 1978; Moscow: Mir, 1981) Vol. 1.
10. Ivanov A.V., Kurnosov V.D., Kurnosov K.V., Chernov R.V. *Zh. Prikl. Spektr.*, **72**, 479 (2005).
11. Minch J., Park S.H., Keating T., Chuang S.L. *IEEE J. Quantum Electron.*, 35, 771 (1999).
12. Olego D., Chang T.Y., Silberg E., et al. *Appl. Phys. Lett.*, **41**, 476 (1982).
13. Kononenko V.K., Manak I.S., Nalivko S.V., et al. *Zh. Prikl. Spektr.*, **64**, 221 (1997).
14. Dutta N.K. *J. Appl. Phys.*, **53**, 7211 (1982).
15. Wilcox J.Z., Ou S., Yang J.J., Jansen M., Peterson G.L. *Appl. Phys. Lett.*, **55**, 825 (1989).
16. Suemutsu Y., Adams A.R. *Handbook of Semiconductor Lasers and Photonic Integrated Circuits* (London: Chapman and Hall, 1994).
17. Yamada M. *J. Appl. Phys.*, **66**, 81 (1989).
18. Kononenko V.K., Manak I.S., Shevtsov V.A. *Fiz. Tekh. Poluprovodn.*, **31**, 1087 (1997).
19. Saint-Cricq B., Lores-Dupuy F., Vassilieff G. *IEEE J. Quantum Electron.*, **22**, 625 (1986).
20. Kurnosov V.D., Kurnosov V.K. *Zh. Prikl. Spektr.*, **67**, 536 (2000).
21. Zhuravleva O.V., Kiseleva N.N., Kurnosov V.D., et al. *Kvantovaya Elektron.*, **21**, 205 (1994) [*Quantum Electron.*, **24**, 187 (1994)].
22. Landsberg P.T., Abrahams M.S., Osinski M. *IEEE J. Quantum Electron.*, 21, 24 (1985).
23. Zhuravleva O.V., Kurnosov V.D., Kurnosov K.V., et al. *Kvantovaya Elektron.*, **34**, 15 (2004) [*Quantum Electron.*, **34**, 15 (2004)].
24. Tomita A., Suzuki A. *IEEE J. Quantum Electron.*, **23**, 1155 (1987).
25. Klinman D.A., Müller R.C. *Phys. Rev. B*, **32**, 2266 (1985).
26. Blood P., Colak S., Kucharska A.I. *IEEE J. Quantum Electron.*, **24**, 1593 (1988).
27. Bennett B.R., Soref R.A., Del Alamo J.A. *IEEE J. Quantum Electron.*, **26**, 113 (1990).
28. Hsu C-F., Zory P.S., Wu C-H., Emanuel M.A. *IEEE J. Selected Topic Quantum Electron.*, **3**, 158 (1997).